Article

Unveiling key descriptors for electrical resistivity of alloys using high-throughput experiments and explainable AI

Check for updates

Taeyeop Kim & Dongwoo Lee ✉

This study examines the electrical resistivity of metals and binary, ternary alloy thin films across a broad range of compositions and microstructures through data-driven approaches. Electrical resistivity values for over 70,000 alloy compositions were measured through high-throughput experiments on combinatorially synthesized specimens. A machine learning prediction model was developed, and an explainable artificial intelligence (XAI) algorithm was utilized to identify the key features influencing electrical resistivity. The results demonstrate that the average valence electron concentration (VEC_{avg}) is the most significant descriptor governing the electrical resistivity of these alloys. Electronegativity difference (ΔEN) and mixing entropy (ΔS) were identified as collaborative features contributing to resistivity. The relationships between these features and resistivity are discussed in the context of traditional theoretical frameworks to provide a comprehensive understanding of the electrical behavior of alloys.

Electrical resistivity of alloys is one of the most important physical properties to be considered for designing the interconnects in integrated circuit chips, as well as electrical conductors, electrical resistors, and microelectromechanical systems (MEMS) devices[1-3]. Additionally, electrical resistivity provides insight into thermal properties and microstructures of metals and alloys[4-7]. For a deeper understanding, theoretical models have been suggested and revealed the fundamentals of electrical resistivity. For instance, Drude model describes that the electrical resistivity is inversely proportional to electron density and relaxation time:

$$\rho = \frac{m}{ne^2\tau} \tag{1}$$

where ρ is the electrical resistivity, m is the electron mass (9.11×10^{-31} kg), n is the number of electrons per unit volume, e is the electron charge (1.6×10^{-19} C), and τ is the relaxation time for an electron between collisions[8]. Matthiessen's rule considers the increase in resistivity resulting from electron scattering events:

$$\rho_{total} = \sum_{i=1}^{N} \rho_i \tag{2}$$

where ρ_{total} is the total electrical resistivity or measured electrical resistivity, N is the total number of electron scattering events, and ρ_i is the electrical resistivity by i^{th} scattering event[9]. Mayadas and Shatzkes (MS),

Fuchs and Sondheimer (FS), and Nordheim's models provide more detailed descriptions of electron scattering mechanisms by taking into account microstructural and chemical features such as grain boundaries, precipitations, phases, vacancies, interstitials, solutes, and their effects on resistivity[10-13].

These models, however, are limited in describing the electrical resistivities of high-solute concentration regions in complex concentrated alloys (CCAs) or multi-component alloys (MCAs), which have gained attention for their exceptional properties[14,15]. It is challenging to capture the behavior of CCAs due to multiple principal elements with unique properties. For instance, a high concentration of solutes in these alloys can induce short-range ordering and amorphization in alloys, which reduce the electron mean free path and contribute to the increase in electrical resistivity[16,17]. Additionally, explaining the electrical resistivity of magnetic CCAs is challenging due to the distinct electron behaviors caused by spin disordering in ferromagnetic alloys and the absence of magnetic scattering in refractory alloys[18,19].

Data-driven and machine learning-based approaches have demonstrated their effectiveness in overcoming challenges associated with analyzing the characteristics of multi-component alloys[20-24]. These approaches have facilitated the development of prediction models for various alloy properties, contributing to the discovery of new alloys with enhanced properties[21,22,25]. However, machine learning models are often regarded as black box models due to their inability to provide clear explanations of the relationships between input features and output. While conventional

School of Mechanical Engineering, Sungkyunkwan University, Suwon, 16419, Republic of Korea. ✉e-mail: dongwoolee@skku.edu

1

correlation analyses like Pearson and Spearman correlations can quantify the importance of each input feature in linear models, they are limited in describing non-linear relationships[26,27]. To address this challenge, ensemble models have been employed to extract the importance of features across the dataset, providing insights into the influence of individual features on model predictions[28]. Additionally, explainable artificial intelligence (XAI) algorithms are capable of quantifying the contributions of input features to the output, thereby facilitating a better understanding of their relationship[29,30].

In this work, we developed a machine learning based electrical resistivity prediction model using an experimental dataset for tens of thousands of alloys obtained from high-throughput resistivity measurements. Subsequently, explainable artificial intelligence was employed to elucidate the relationship between input features and electrical resistivity, as well as to determine descriptors. We adopted the integrated gradients algorithm, which reveals the contribution of input features to the output by aggregating the gradients of inputs[31]. Finally, the descriptors for electrical resistivity, which describe the dissimilarities in the electrical resistivity of the constituent elements, have been characterized.

Results

Experimental data acquisition
The construction of the electrical resistivity prediction model commenced with the acquisition of experimental data on electrical resistivity from thin-film metals and alloys. To ensure high model performance, it is crucial to gather a large amount of property data[32]. We employed combinatorial synthesis (Fig. 1a) using a magnetron co-sputtering system, a technique that produces a composition spread on a single wafer by controlling the powers of multiple guns and depositing without substrate rotation[5,6,33,34]. Then, high-throughput (HT) experiments were conducted, facilitating the rapid acquisition of electrical resistivity data through the utilization of the $X–Y$ robotics stage (Fig. 1b, c)[5,33]. By utilizing this method, thin-film alloys can be synthesized under nearly consistent conditions, facilitating the collection of data that is more suitable for machine learning training. Further details of the electrical property measurements are provided in *Methods* section.
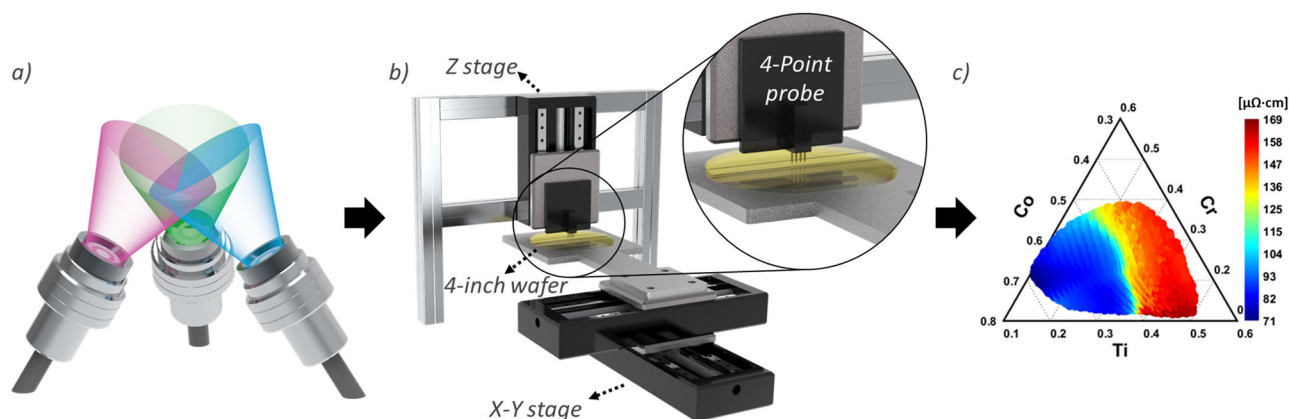
Datasets
For machine learning and XAI analysis, we curated a comprehensive dataset of electrical resistivity values from high-throughput (HT) experiments on a diverse array of thin-film alloys, encompassing 6 pure metals, 7 binary systems, and 30 ternary systems (Table S1). The composition distribution across these alloys is depicted in the swarm plot (Fig. 2a), where each data point represents an experimental composition by its atomic concentration, highlighting the dataset's compositional diversity essential for robust machine learning modeling. To extend the applicability of our model

toward CCAs, several ternary alloys in this study were intentionally designed with relatively high solute concentrations—often exceeding 20 at.% per element—to emulate the chemical complexity and configurational disorder characteristic of multi-principal element systems. In Fig. 2b, the violin plot illustrates the resistivity distribution for alloys based on their primary element, where the width of each plot denotes the density of data points at different resistivity levels. Figure 2c presents a histogram of resistivity values across all data, revealing multiple peaks, with the most prominent around 120 $\mu\Omega\cdot$cm, and additional peaks near 50 and 220 $\mu\Omega\cdot$cm. This peak distribution demonstrates the dataset's breadth in resistivity variation, offering rich insights into the electrical properties of alloys. The stacked bar charts (Fig. 2d–f) further categorize the data by alloy type. While the binary alloy data (7190 data points) exhibit limited diversity, the predominance of ternary alloys (64,348 data points) highlights their compositional flexibility and suitability for exploratory analysis. This extensive and varied dataset provides a solid foundation for machine learning and XAI to analyze electrical resistivity across a wide spectrum of ternary alloy compositions, supporting a detailed examination of feature importance and enabling novel insights into alloy design.
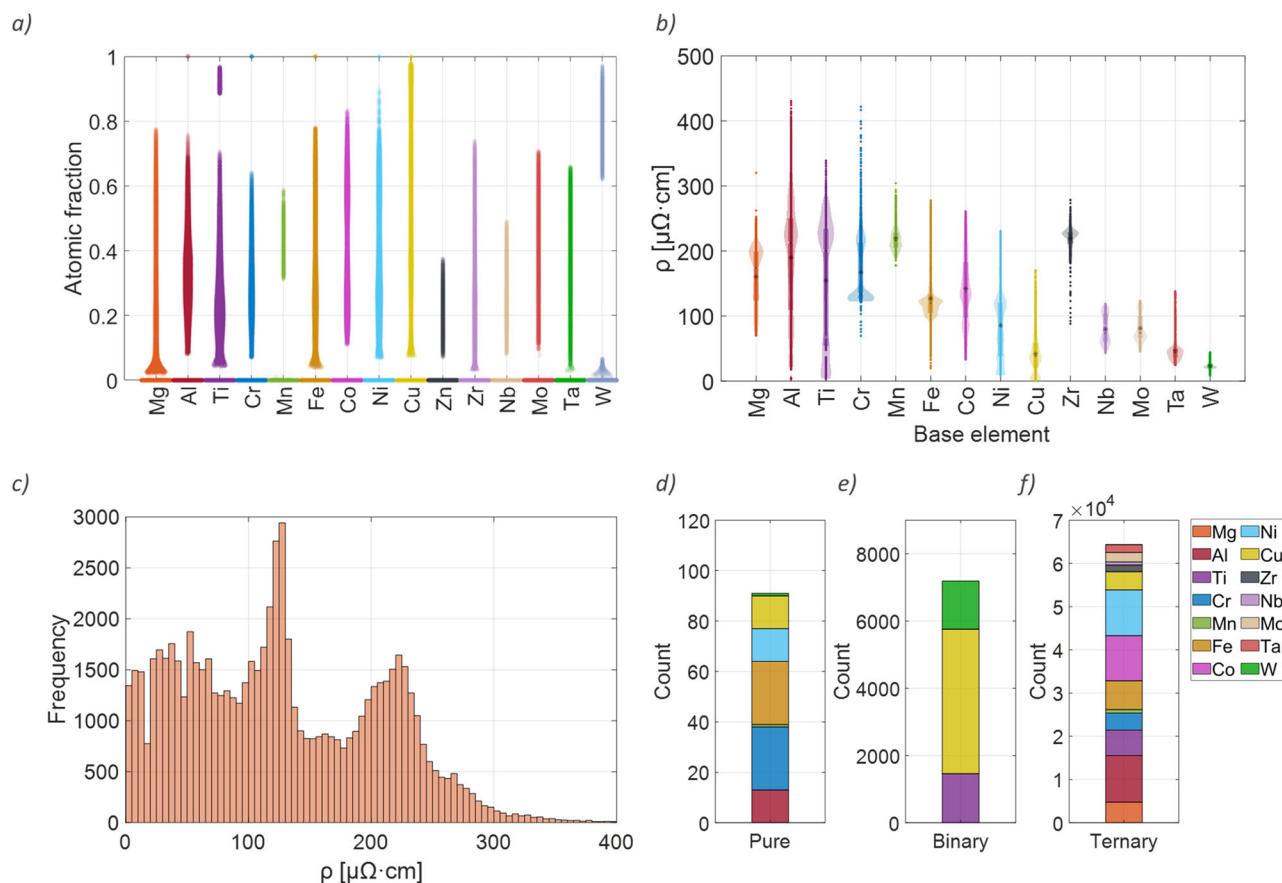
Feature selection
To predict electrical resistivity, we developed an artificial neural network (ANN) model, which effectively captures the complex non-linear relationships between input features and resistivity. The electrical resistivity values obtained from high-throughput (HT) experiments were used as the model outputs. The model incorporates both intrinsic and extrinsic input parameters that influence alloy microstructure and resistivity. The intrinsic parameters, directly related to the alloy's atomic structure and bonding characteristics, include the average atomic radius (r_{avg}), which correlates with the relaxation time of free electrons and thereby affects electron mobility in the alloy matrix[35–38]. The average valence electron concentration (VEC_{avg}) was included to represent electron density, which plays a crucial role in conductivity[39,40]. Additionally, atomic radius mismatch (δ) and mixing entropy (ΔS) were incorporated to capture local lattice distortions and chemical disorder, both of which impact electron scattering within the alloy[13,41]. Other intrinsic parameters, such as electronegativity difference (ΔEN) and heat of mixing (ΔH_{mix}), were also selected because of their relevance to microstructural phase stability: a higher ΔEN promotes compound formation, while smaller values of ΔH_{mix} tend to favor the formation of disordered crystalline phases[42,43].

To account for variations arising from the sputter deposition process, extrinsic parameters affecting the microstructure and impurity concentration were also included. Film thickness (t), measured through cross-sectional scanning electron microscopy (SEM), and homologous temperature (T_h), defined as the ratio of the deposition temperature to the rule of

Fig. 1 | Schematic illustration of the combinatorial electrical resistivity data acquisition process. a Combinatorial alloy fabrication through physical vapor deposition. **b** High-throughput robotic electrical resistivity data acquisition using a 4-probe resistance mapper. **c** An example of electrical resistivity map of the measured combinatorially sputter deposited thin-film alloys.

Fig. 2 | Alloy compositions and electrical resistivity distributions across pure metals, binary alloys, and ternary alloys. a Swarm plot showing the distribution of compositions in the training data. **b** Violin plot depicting the distribution of electrical resistivity data based on base elements. The asterisk within each violin indicates the mean resistivity for each alloy group, and the width highlights the density of resistivity values. **c** Histogram of the number of resistivity data points across all datasets. Stacked bar plots of the distribution of electrical resistivity data of (**d**) pure metals, (**e**) binary alloys, and (**f**) ternary alloys, labeled by base elements.

mixture melting point, were incorporated for their influence on grain size and grain boundary density, which significantly affect electron scattering and resistivity[44,45]. Additionally, the deposition rate (v_d) was included to represent impurity levels in vapor-deposited films, as lower deposition rates generally increase resistivity through enhanced electron-impurity scattering[46,47]. Detailed formulas used for calculating these features are provided in Table 2 in the *Methods* section, outlining each parameter's derivation from alloy compositions and atomic properties.
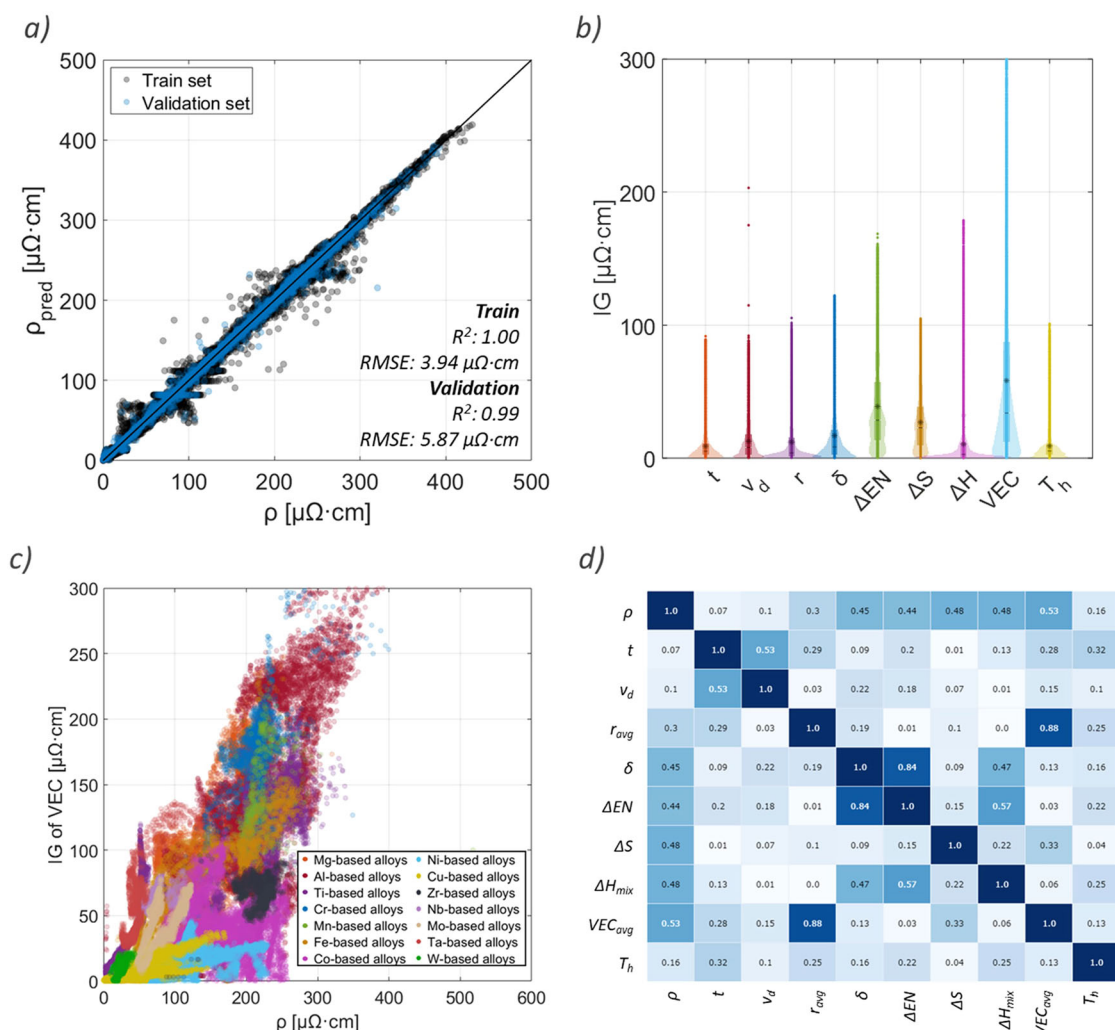
Machine learning modeling

Figure 3a illustrates the performance of the trained ANN model for the training and validation sets, demonstrating its high predictive accuracy for electrical resistivity. The model achieved an R^2 of 1.00 with a root mean square error (RMSE) of 3.94 $\mu\Omega$ cm on the training set, and an R^2 of 0.99 with an RMSE of 5.86 $\mu\Omega$ cm on the validation set (see *Methods* for modeling details). To further validate the generalizability of our model, we conducted an additional evaluation on four independent quaternary alloy systems (5,744 datapoints for Al–Ti–Co–Ni, Cr–Fe–Co–Ni, Cr–Mn–Co–Ni, and Ti–Nb–Ta–W), tabulated in Table S2. The prediction results (Fig. S1) show high accuracy, with an RMSE of 31.9 $\mu\Omega$ cm across these systems. This result demonstrates the model's effectiveness in capturing the relationship between input features and electrical resistivity, even for quaternary systems.

Figure 3b displays violin plots of feature importance values across the entire dataset, with asterisks indicating the average IG values derived using the integrated gradients (IG) method[31] (*Methods*). By using Cu film, the most conductive metal in our dataset, as the baseline, the IG values reflect how much each feature influences resistivity relative to the baseline,

quantitatively explaining why a given alloy exhibits higher resistivity in a physically meaningful way. The XAI results reveal that the average valence electron concentration (VEC_{avg}) is the most significant feature, with a mean importance value of 58.3 $\mu\Omega$·cm. Additionally, Figure S2 illustrates the distributions of feature importance across pure metals, binary alloys, and ternary alloys, further emphasizing the critical role of VEC_{avg} in complex alloy systems. It is noticeable that ΔEN holds high importance in binary (24 $\mu\Omega$·cm) and ternary (40.5 $\mu\Omega$·cm) alloys, as it is a key descriptor associated with chemical disorder and phase formation behavior[19,48].

The feature importance values calculated for each parameter across all alloy groups (Fig. 3c and Fig. S3) reveal that VEC_{avg} exhibits a linear relationship with electrical resistivity. This indicates that higher values of VEC_{avg} correlate with increased resistivity (Fig. 3c), with its influence becoming particularly pronounced in alloys with high resistivity. The features with the next highest average of importance values are electronegativity difference (ΔEN, 38.8 $\mu\Omega$ cm), followed by mixing entropy (ΔS, 29.4 $\mu\Omega$·cm), and atomic radius mismatch (δ, 16.9 $\mu\Omega$ cm). Other parameters show comparatively lower feature importance values. These findings are somewhat consistent with the absolute Pearson correlation coefficients in Fig. 3d, which indicate high correlation values (>0.4) for the intrinsic parameters VEC_{avg}, δ, ΔEN, ΔS, and ΔH_{mix}.

Both the XAI and Pearson correlation analyses suggest that extrinsic parameters, such as thickness (t), homologous temperature (T_h), and deposition rate (v_d), have a lower impact on electrical resistivity. The data distributions in Fig. S4 support these findings. For example, thickness values (Fig. S4a) are predominantly concentrated around 510 nm, except in Cu and W thin-film alloys. Similarly, deposition rates (Fig. S4b) mostly fall within 0.2 to 0.35 nm/s, resulting in limited impurity variation across films[49].

Fig. 3 | Model performance and explainable AI results. a Prediction model performance with R^2 and RMSE values. **b** Violin plots of feature importance determined by XAI for the total dataset. Asterisks indicate the average feature importance values. **c** Feature importance (IG) values of average valence electron concentration vs. electrical resistivity. **d** Absolute Pearson correlation coefficients for the input features and electrical resistivity (ρ) of the machine learning model.

Fig. 4 | Relationship between descriptors and electrical resistivity. VEC_{avg} versus electrical resistivity (ρ) for the metals and alloys color-coded by (**a**) base elements, (**b**) electronegativity difference (ΔEN).
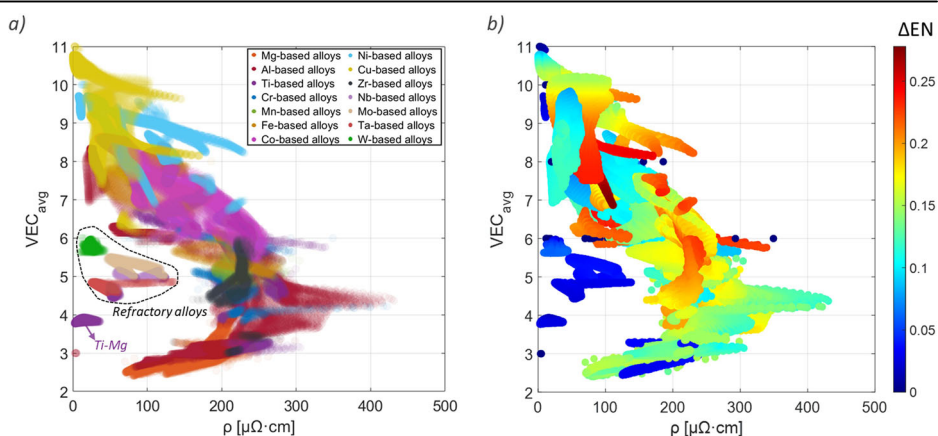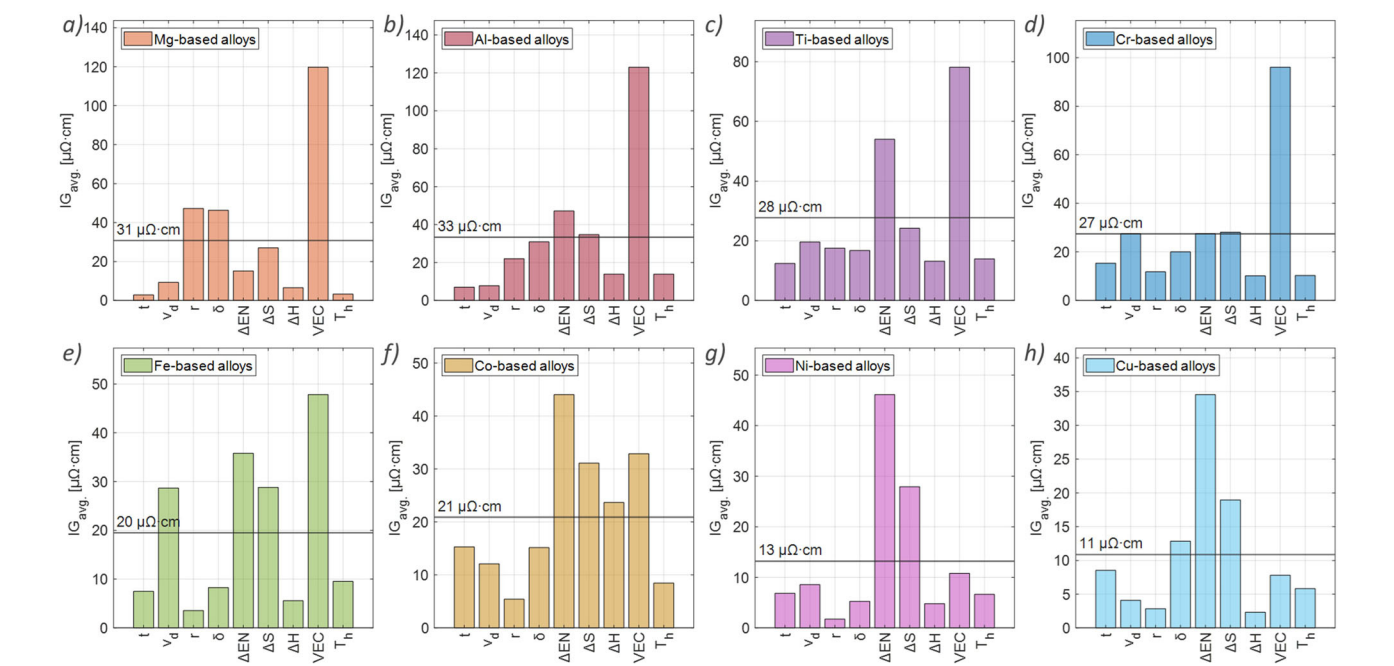
Table S3 lists the standard deviation of normalized feature values and illustrates the relatively small values of 0.24 and 0.18 for thickness and deposition rate, respectively. Moreover, the majority of homologous temperature values (Fig. S4i) for combinatorial thin films are lower than 0.5, indicating small grain formation according to the structure zone model[45].

The limited variations in extrinsic factors reinforce the dominant role of intrinsic parameters in determining electrical resistivity.

Figure 4a illustrates the relationship between VEC_{avg} and electrical resistivity. In the low-VEC_{avg} region (2–4), alloys with base elements of Mg, Al, and low-VEC transition metals exhibit an increase in resistivity with

Fig. 5 | Feature importance analysis for each alloy group. Average feature importance values of (**a**) Mg-, (**b**) Al-, (**c**) Ti-, (**d**) Cr-, (**e**) Fe-, (**f**) Co-, (**g**) Ni-, and (**h**) Cu-based thin-film alloys. The solid line and its corresponding value represent the average of the total feature importance (IG) values for each alloy group.

Table 1 | Descriptors of each alloy group in the order of the mean feature importance values

Base element	Feature 1	Feature 2	Feature 3	Feature 4
Mg	VEC_{avg} (120 μΩ·cm)	r_{avg} (47 μΩ cm)	δ (46 μΩ cm)	
Al	VEC_{avg} (123 μΩ·cm)	ΔEN (47 μΩ cm)	ΔS (35 μΩ cm)	
Ti	VEC_{avg} (78 μΩ·cm)	ΔEN (54 μΩ cm)		
Cr	VEC_{avg} (96 μΩ·cm)	ΔS (28 μΩ cm)	ΔEN (28 μΩ cm)	v_d (28 μΩ cm)
Fe	VEC_{avg} (69 μΩ·cm)	ΔEN (48 μΩ cm)	ΔS (29 μΩ cm)	v_d (28 μΩ cm)
Co	ΔEN (44 μΩ·cm)	VEC_{avg} (33 μΩ cm)	ΔS (31 μΩ cm)	ΔH_{mix} (24 μΩ cm)
Ni	ΔEN (46 μΩ·cm)	ΔS (28 μΩ cm)		
Cu	ΔEN (35 μΩ·cm)	ΔS (19 μΩ cm)	δ (13 μΩ cm)	

rising VEC_{avg}. In these alloys, electronic conduction primarily occurs through s-electrons. The positive relationship between VEC_{avg} and resistivity can be attributed to the enhanced scattering of s-electrons, influenced by an increased number of vacant s- and d-states introduced through alloying[50,51]. In systems with a limited number of conduction electrons, a higher density of grain boundaries and lattice distortions from alloying further intensify electron scattering, contributing to higher resistivity.

In the regime where VEC_{avg} is greater than 4, typically dominated by transition metals like Co, Ni, and Cu, resistivity decreases with increasing VEC_{avg}. In these metals, conduction is facilitated by both s- and d-electrons. As VEC_{avg} increases, the d-band progressively fills, reducing the number of unfilled states available for electron scattering. This reduction in scattering states, combined with stronger metallic bonding, lower overall electron scattering, and higher free electron density, results in a decrease in electrical resistivity.

Some alloy systems deviate from the general trend between VEC_{avg} and electrical resistivity described above. As shown in Fig. 4a, alloys such as Ti–Mg, Ti–Nb–Ta, Ti–Nb–Mo, and W–Ta, which fall within the mid-VEC_{avg} range (4–6), exhibit lower resistivity than other thin-film alloys with similar VEC_{avg} values. This deviation is likely attributed to the very small electronegativity difference (<0.07) in these alloys (Fig. 4b). A larger electronegativity attracts the electron with a local charge transfer and promotes the intermetallic compound formation which are associated with directional

chemical bonding inhomogeneities among alloying elements[42,52,53]. The minimal electronegativity differences in these alloys reduce the likelihood of such compound formation, enhancing electron transport. Furthermore, these alloys exhibit very small atomic radius mismatches (0.2–2.7%) (Fig. S5a), leading to minimal lattice distortion and reduced electron scattering. Additionally, a small absolute heat of mixing ($|\Delta H_{mix}|$) values (Fig. S5b) for Ti–Mg (1.9–6.5 kJ/mol), Ti–Nb–Ta (0.58–4.53 kJ/mol), Ti–Nb–Mo (2.7–4.8 kJ/mol), and W–Ta (0.7–6.6 kJ/mol) fall within the solid-solution zone suggested by Zhang et al.[48]. This indicates a tendency for these alloys to form homogeneous solid solutions rather than complex intermetallic phases, further contributing to their lower resistivity.

To provide system-dependent insights into how descriptor importance varies across different alloy types, we categorized the feature importance values derived from the trained model based on the base elements. For consistency, the base element was defined as the element with the highest atomic fraction in each alloy. From the original dataset, we excluded Mn-, Zr-, Nb-, Mo-, Ta-, and W-based thin-film alloys due to their limited data (<2500 entries) and diversity (< 4 systems), as well as their restricted feature distributions (see Fig. S4 and Table S1). For each alloy group, two to four features exhibit higher importance than the average total feature importance value, as shown in Fig. 5 and Table 1.

The average valence electron concentration (VEC_{avg}) is identified as the most significant feature across most alloy groups, demonstrating its

universal relevance in alloy characterization. The relatively lower importance of VEC_{avg} in Ni- and Cu-based alloys can be attributed to the inherently high VEC values of the base elements (e.g., Ni: 10, Cu: 11), which makes it challenging to differentiate these alloys from the baseline of pure Cu film. Electronegativity difference (ΔEN), which contributes to chemical disorder and influences phase stability, is also significant for most alloy groups. An exception is observed in Mg-based alloys (Fig. 5a), where the impact of ΔEN is less pronounced due to the exceptionally low electronegativity of Mg (1.293) compared to the average of 3 d transition metals (1.65), which promotes its tendency to form compounds when alloyed with most transition metals[54,55].

Mixing entropy (ΔS), which captures chemical disorder independent of elemental characteristics related to solid-solution effects and Nordheim's rule, stands out as an influential feature for Al-, Cr-, Fe-, Co-, Ni-, and Cu-based alloys. Atomic radius mismatch (δ), which is known to affect amorphization and lattice distortion, notably contributes significantly to the resistivity of Mg- and Cu-based thin films (Fig. 5a, h)[43,56]. These base elements exhibit either notably smaller atomic size (Cu: 1.276 Å) or larger atomic size (Mg: 1.598 Å) compared to the average atomic radius of 3 d transition metals (1.336 Å). Especially, the significantly large atomic size of Mg, which exhibits the largest r_{avg} values among all alloys studied (Fig. S4c), enhances the role of r_{avg} in determining the electrical resistivity of Mg-based alloys, as evidenced in Fig. 5a.

The heat of mixing (ΔH_{mix}) proves to be a crucial feature for Co-based alloys. High absolute ΔH_{mix} values in Co-(Al, Ti, Zr), ranging from 19 to 41 kJ/mol, suggest that ΔH_{mix} impedes the formation of disordered solid solutions, consistent with findings from previous studies[57]. This implies that higher ΔH_{mix} values reduce the likelihood of disordered solid solution, thereby affecting resistivity. Furthermore, deposition rate (v_d), which reflects impurity concentration in films, has emerged as an important feature for Cr- and Fe-based alloys[58]. The relatively high melting temperatures of Cr and Fe (e.g., Cr: 2180 K, Fe: 1811 K) compared to the average melting point of 3d transition metals (1699 K) limit atomic diffusion and make their resistivity more sensitive to the deposition rate [47].

To verify the descriptor features (Table 1) for each alloy group, electrical resistivity models with two to four features were constructed and trained. The identical model structure used for training the total dataset was employed, with the input dimension adjusted according to the number of descriptors listed in Table1 for each alloy group (from nine to the specified number of features). Figure S6 and S7 present the results for these models, demonstrating high accuracy across all alloy groups, with RMSE values below 11.7 μΩ·cm and R^2 values exceeding 0.86. Notably, despite being trained with fewer features than the unified model with nine features (Fig. 3a), these models effectively predict the electrical resistivity of thin-film alloys.

Discussion

In this study, we developed a machine-learning model to predict the electrical resistivity of thin-film alloys and applied the integrated gradients (IG) method to identify key descriptors impacting resistivity. Our analysis revealed that average valence electron concentration (VEC_{avg}) is the most influential descriptor, demonstrating its importance across alloy systems. Collaborative phase-determining parameters, such as electronegativity difference (ΔEN) and mixing entropy (ΔS), also play critical roles, collectively affecting resistivity. Additionally, unique atomic characteristics intrinsic to each base element influence the importance of specific descriptors within alloy groups. For instance, atomic radius mismatch (δ) is significant in Mg- and Cu-based alloys, while average atomic radius (r_{avg}) is especially relevant in Mg-based alloys. The heat of mixing (ΔH_{mix}) notably influences Co-based alloys, reflecting its role in stabilizing disordered solid solutions. These findings provide valuable insights into the complex factors governing electrical resistivity in multi-component alloys. While this study demonstrated the applicability of the prediction model to quaternary alloy systems, the same data-driven strategy may be extended to higher-order alloys, with further validation needed to confirm its robustness across broader compositional spaces.

Methods

Electrical resistivity measurement

We employed a scanning 4-probe measurement technique to measure the resistance distribution across the combinatorially synthesized thin-film alloys[6]. Current (I) was driven through current probes, and the voltage difference (V) was precisely gauged using a digital multimeter (DM3058e, RIGOL). The recorded sheet resistance data, obtained by dividing the voltage by the current, were subsequently adjusted utilizing Eq. (3)[59]:

$$\rho = FRt \qquad (3)$$

where ρ is the electrical resistivity, F is the correction factor of 4.5324 for a 4-inch circular specimen, R is the measured resistance, and t is the film thickness.

Semi-empirical features for machine learning models

Intrinsic features for model training were calculated based on the compositions of the thin-film alloys and atomic properties (Table S4)[60,61]. The parameters used for the machine learning model can be calculated by the formulas in Table 2. C_i, VEC_i, r_i, EN_i and T_{mi} are atomic concentration, valence electron concentration, atomic radius, electronegativity, and melting temperature of ith element, respectively. ΔH_{ij}^{mix} is the mixing enthalpy between i^{th} and j^{th} elements, which is calculated by Miedema's model[43].

Machine learning model details

An artificial neural network (ANN) model was developed to predict electrical resistivity, with the optimal architecture determined through a grid search. This process involved constructing models using all combinations of hidden layers (1 to 4) and nodes per layer (128, 256, 512, 1024, and 2048). This systematic search allowed us to evaluate each model configuration and select the one that yielded the best performance for predicting resistivity. Each hidden layer was dropped out with a dropout rate of 0.3, and ReLU was used as the activation function. The dataset was randomly divided, with 10% designated as a validation set. All the ML models in this work were trained using the Adam optimizer with a learning rate of 5×10^{-4}. The nine selected features (Table 2) were normalized between 0 and 1 before training. For reproducibility, the random seed and the training epoch were set to 42 and 2000, respectively. To prevent overfitting, we continuously monitored the validation loss during training and saved the model at the epoch where the validation loss reached its minimum, which occurred at epoch 1926 (Fig. S8). As shown in Fig. S9, the architecture with 3 hidden layers and 512 nodes achieved the lowest validation RMSE of 5.87 μΩ cm, establishing it as the optimal configuration for accurate resistivity predictions. Subsequently, we

Table 2 | Formulas for input feature preparation for model construction[25]

Parameter	Formula	Description
r_{avg}	$\sum_{i=1}^{n} C_i r_i$	Average atomic radius
δ	$\sqrt{\sum_{i=1}^{n} C_i (1 - \frac{r_i}{r_{avg}})^2}$	Atomic radius mismatch
ΔEN	$\sqrt{\sum_{i=1}^{n} C_i (\sum_{j=1}^{n} C_j EN_j - EN_i)^2}$	Electronegativity difference
ΔS	$-R \sum_{i=1}^{n} C_i \ln(C_i)$	Mixing entropy
ΔH_{mix}	$\sum_{i=1, j>i}^{n} 4 C_i C_j \Delta H_{ij}^{mix}$	Heat of mixing
VEC_{avg}	$\sum_{i=1}^{n} C_i VEC_i$	Average valence electron concentration
T_h	$T_{deposition} / \sum_{i=1}^{n} C_i T_{mi}$	Homologous temperature

unveiled the descriptor feature for electrical resistivity using the integrated gradients (IG) method. IG method determines the feature importance by calculating the gradients of input features. The feature importance of ith feature (IG_i) for each alloy composition can be defined as Eq. (4)[31]:

$$IG_i \approx |(x_i - x_i') \times \sum_{m=1}^{M} \frac{\partial F(x' + \frac{m}{M}(x - x'))}{\partial x_i} \times \frac{1}{M}| \qquad (4)$$

where $x \in \mathbb{R}^d$ is the input feature vector with dimension $d = 9$, x_i is the ith feature of input x, $x' \in \mathbb{R}^d$ is the baseline input, M is the number of steps for the Riemann sum approximation of the integral (set to 30 in this study), and $\frac{\partial F(x)}{\partial x_i}$ is the gradient of the model output $F(x)$ with respect to the ith feature. We used the input feature of Cu as the baseline x' to analyze the contribution of each input feature to increases in electrical resistivity. Using Cu as a baseline allows us to assess the specific impact of each input feature in the alloy on the overall electrical resistivity, providing deeper insights into the role of individual alloying elements.

Data availability

The authors declare that the main data supporting the findings of this study are available within the article and its Supplementary material file. All other relevant data are available from the corresponding author upon reasonable request.

Code availability

The pre-trained model for predicting the electrical resistivity of alloys, along with the code used for inference, is available via https://github.com/TaeyeopK/ML-for-Electrical-Resistivity-of-Alloys.

References

1. Sim, G.-D. et al. Nanotwinned metal MEMS films with unprecedented strength and stability. *Sci. Adv.* **3**, e1700685 (2017).
2. Gall, D. The search for the most conductive metal for narrow interconnect lines. *J. Appl. Phys.* **127** (2020).
3. Huo, W. et al. Ultrahigh hardness and high electrical resistivity in nano-twinned, nanocrystalline high-entropy alloy films. *Appl. Surf. Sci.* **439**, 222–225 (2018).
4. Klemens, P. & Williams, R. Thermal conductivity of metals and alloys. *Int. Met. Rev.* **31**, 197–215 (1986).
5. Jo, H., Park, S., You, D., Kim, S. & Lee, D. Combinatorial discovery of irradiation damage tolerant nano-structured W-based alloys. *J. Nucl. Mater.* **572**, 154066 (2022).
6. You, D. et al. Electrical resistivity as a descriptor for classification of amorphous versus crystalline phases of alloys. *Acta Materialia* **231**, 117861 (2022).
7. Khadka, J., Ganorkar, S. & Lee, D. Investigation of thermal emissivity and electrical resistivity of highly reflective nano-grained metal films. *Appl. Therm. Eng.* **268**, 125854 (2025).
8. Rossiter P. L. *The Electrical Resistivity Of Metals And Alloys* (Cambridge University Press, 1991).
9. Matthiessen, A. & Vogt, C. Ueber den Einfluss der Temperatur auf die elektrische Leitungsfähigkeit der Legirungen. *Ann. Phys.* **198**, 19–78 (1864).
10. Fuchs K. The conductivity of thin metallic films according to the electron theory of metals. (ed. Green, B.J.) *Proc. of the Camb. Philos. Soc.* **34**, 100–108 (1938).
11. Mayadas, A. & Shatzkes, M. Electrical-resistivity model for polycrystalline films: the case of arbitrary reflection at external surfaces. *Phys. Rev. B* **1**, 1382 (1970).
12. Yan, X. & Zhang, Y. Functional properties and promising applications of high entropy alloys. *Scr. Materialia* **187**, 188–193 (2020).
13. Nordheim, L. Zur elektronentheorie der metalle. I. *Ann. Phys.* **401**, 607–640 (1931).
14. Miracle, D. B. & Senkov, O. N. A critical review of high entropy alloys and related concepts. *Acta Materialia* **122**, 448–511 (2017).
15. George, E. P., Raabe, D. & Ritchie, R. O. High-entropy alloys. *Nat. Rev. Mater.* **4**, 515–534 (2019).
16. Rossiter, P. Electrical resistivity near the critical point in binary alloys. *J. Phys. F: Met. Phys.* **10**, 1787 (1980).
17. Krempaský, J. A theory of electrical conductivity in metallic glasses. *Czechoslovak J. Phys. B* **28**, 653–662 (1978).
18. Coles, B. Spin-disorder effects in the electrical resistivities of metals and alloys. *Adv. Phys.* **7**, 40–71 (1958).
19. Mu, S., Wimmer, S., Mankovsky, S., Ebert, H. & Stocks, G. M. Influence of local lattice distortions on electrical transport of refractory high entropy alloys. *Scr. Materialia* **170**, 189–194 (2019).
20. Mansouri Tehrani, A. et al. Machine learning directed search for ultraincompressible, superhard materials. *J. Am. Chem. Soc.* **140**, 9844–9853 (2018).
21. Ren, F. et al. Accelerated discovery of metallic glasses through iteration of machine learning and high-throughput experiments. *Sci. Adv.* **4**, eaaq1566 (2018).
22. Sarker, S. et al. Discovering exceptionally hard and wear-resistant metallic glasses by combining machine-learning with high throughput experimentation. *Appl. Phys. Rev.* **9** (2022).
23. Oliynyk, A. O. et al. High-throughput machine-learning-driven synthesis of full-Heusler compounds. *Chem. Mater.* **28**, 7324–7331 (2016).
24. Choi, P. et al. Data-driven investigation of magnetostructural phase distributions in Mn-Fe-Ni-Si-Al alloy library. *J. Alloys Compounds* **1029**, 180739 (2025).
25. Kim, T. et al. Data-driven discovery of ultrahigh specific hardness alloys. *J. Mater. Res. Technol.* **33**, 7753–7760 (2024).
26. Wen, C. et al. Machine learning assisted design of high entropy alloys with desired property. *Acta Materialia* **170**, 109–117 (2019).
27. Jo, H., Moon, H., Kim, J. & Lee D. Enhancing corrosion resistance of Ti-Coated SUS316L bipolar plates: the role of residual stress and microstructural evolution. *Corrosion Sci.* **256**, 113194 (2025).
28. Ramprasad, R., Batra, R., Pilania, G., Mannodi-Kanakkithodi, A. & Kim, C. Machine learning in materials informatics: recent applications and prospects. *npj Comput. Mater.* **3**, 54 (2017).
29. Adadi, A. & Berrada, M. Peeking inside the black-box: a survey on explainable artificial intelligence (XAI). *IEEE access* **6**, 52138–52160 (2018).
30. Kwon, N. et al. Machine learning investigation of high-k metal gate processes for dynamic random access memory peripheral transistor. *APL Mater.* **12** (2024).
31. Sundararajan, M., Taly, A. & Yan, Q. Axiomatic attribution for deep networks. (eds. Precup, D. & Whye, T. Y.) *Proceeding of Machine Learning Research* **70**, 3319–3328 (2017).
32. Hestness, J., Ardalani, N. & Diamos, G. Beyond human-level accuracy: Computational challenges in deep learning. (ed. Hollingsworth, J.) *Proceedings of the 24th Symposium on Principles and Practice of Parallel Programming*, 1–14 (Association for Computing Machinery, 2019).
33. Kim, K. et al. Mechanical, electrical properties and microstructures of combinatorial Ni-Mo-W alloy films. *J. Alloy Compd.* **919**, 165808 (2022).
34. Song, J., Jo, H., Kim, T. & Lee, D. Experimental data management platform for data-driven investigation of combinatorial alloy thin films. *APL Materials* **11** (2023).
35. Kokanović, I. Effect of disorder on the electrical resistivity in the partially crystalline Zr76Ni24 metallic glasses. *J. Alloys Compunds* **421**, 12–18 (2006).
36. Mu, S., Pei, Z., Liu, X. & Stocks, G. M. Electronic transport and phonon properties of maximally disordered alloys: from binaries to high-entropy alloys. *J. Mater. Res.* **33**, 2857–2880 (2018).

37. Allen, P. B. Metals with small electron mean-free path: saturation versus escalation of resistivity. *Phys. B: Condens. Matter* **318**, 24–27 (2002).

38. Li, L., Lin, S.-T., Dong, C. & Lin, J.-J. Electron-phonon dephasing time due to the quasistatic scattering potential in metallic glass CuZrAl. *Phys. Rev. B* **74**, 172201 (2006).

39. Guo, S., Ng, C., Lu, J. & Liu, C. Effect of valence electron concentration on stability of fcc or bcc phase in high entropy alloys. *J. Appl. Phys.* **109**, (2011).

40. Wang, J. et al. Effect of the valence electron concentration on the yield strength of Ti–Zr–Nb–V high-entropy alloys. *J. Alloys Compounds* **868**, 159190 (2021).

41. Zhang, Y. et al. Influence of chemical disorder on energy dissipation and defect evolution in concentrated solid solution alloys. *Nat. Commun.* **6**, 8736 (2015).

42. Singh, A. K. & Subramaniam, A. On the formation of disordered solid solutions in multi-component alloys. *J. Alloys Compounds* **587**, 113–119 (2014).

43. Takeuchi, A. & Inoue, A. Classification of bulk metallic glasses by atomic size difference, heat of mixing and period of constituent elements and its application to characterization of the main alloying element. *Mater. Trans.* **46**, 2817–2829 (2005).

44. Dulmaa, A., Cougnon, F. G., Dedoncker, R. & Depla, D. On the grain size-thickness correlation for thin films. *Acta Materialia* **212**, 116896 (2021).

45. Thompson, C. V. Structure evolution during processing of polycrystalline films. *Annu. Rev. Mater. Sci.* **30**, 159–190 (2000).

46. Cougnon, F., Dulmaa, A., Dedoncker, R., Galbadrakh, R. & Depla, D. Impurity dominated thin film growth. *Appl. Phys. Lett.* **112** (2018).

47. Kim, T. & Lee, D. Microstructures, electrical and mechanical properties of the magnetron sputter deposited metal thin films at variable angles. *Thin Solid Films* **802**, 140438 (2024).

48. Zhang, Y., Zhou, Y. J., Lin, J. P., Chen, G. L. & Liaw, P. K. Solid-solution phase formation rules for multi-component alloys. *Adv. Eng. Mater.* **10**, 534–538 (2008).

49. Alvarez, R. et al. On the deposition rates of magnetron sputtered thin films at oblique angles. *Plasma Process. Polym.* **11**, 571–576 (2014).

50. Wei, C., Antolin, N., Restrepo, O. D., Windl, W. & Zhao, J.-C. A general model for thermal and electrical conductivity of binary metallic systems. *Acta Materialia* **126**, 272–279 (2017).

51. Lilly, A., Deevi, S. & Gibbs, Z. Electrical properties of iron aluminides. *Mater. Sci. Eng. A* **258**, 42–49 (1998).

52. Zhang, Y., Osetsky, Y. N. & Weber, W. J. Tunable chemical disorder in concentrated alloys: defect physics and radiation performance. *Chem. Rev.* **122**, 789–829 (2021).

53. Hu, Q., Guo, S., Guo, J., Luo, F. & Wang, J. Effect of Mo on high-temperature strength of refractory complex concentrated alloys: A perspective of electronegativity difference. *J. Alloys Compounds* **906**, 164186 (2022).

54. Miedema, A. The electronegativity parameter for transition metals: heat of formation and charge transfer in alloys. *J. Less Common Met.* **32**, 117–136 (1973).

55. Abaspour, S. & Cáceres, C. H. Thermodynamics-based selection and design of creep-resistant cast Mg alloys. *Metall. Mater. Trans. A* **46**, 5972–5988 (2015).

56. Li, L. et al. Lattice-distortion dependent yield strength in high entropy alloys. *Mater. Sci. Eng. A* **784**, 139323 (2020).

57. Yang, X. & Zhang, Y. Prediction of high-entropy stabilized solid-solution in multi-component alloys. *Mater. Chem. Phys.* **132**, 233–238 (2012).

58. Learn, A. J. & Foster, D. W. Resistivity, grain size, and impurity effects in chemically vapor-deposited tungsten films. *J. Appl. Phys.* **58**, 2001–2007 (1985).

59. Vaughan, D. Four-probe resistivity measurements on small circular specimens. *Br. J. Appl. Phys.* **12**, 414 (1961).

60. Pauling, L. Atomic radii and interatomic distances in metals. *J. Am. Chem. Soc.* **69**, 542–553 (1947).

61. Allen, L. C. Electronegativity is the average one-electron energy of the valence-shell electrons in ground-state free atoms. *J. Am. Chem. Soc.* **111**, 9003–9014 (1989).

Author contributions

T.K. and D.L. conceived and designed the experiments and machine learning models, which were carried out by T.K. D.L. supervised the project and acquired funding to support the research. T.K. and D.L. wrote the manuscript, and all authors contributed to data analysis and provided comments on the manuscript.

Competing interests

The authors declare no competing interests.

Additional information

Supplementary information The online version contains supplementary material available at https://doi.org/10.1038/s41524-025-01799-9.

Correspondence and requests for materials should be addressed to Dongwoo Lee.

Reprints and permissions information is available at http://www.nature.com/reprints

Publisher's note Springer Nature remains neutral with regard to jurisdictional claims in published maps and institutional affiliations.